

Light-Activated Nuclear Translocation of Adeno-Associated Virus Nanoparticles Using Phytochrome B for Enhanced, Tunable, and Spatially Programmable Gene Delivery

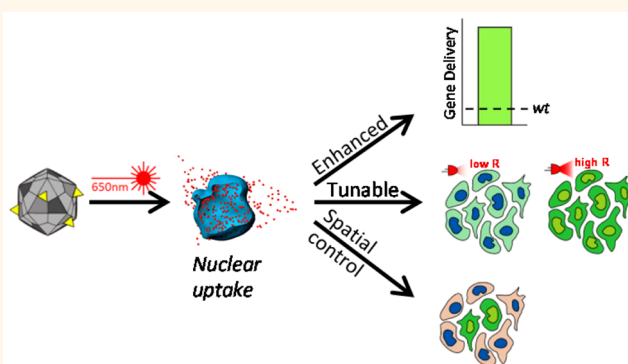
Eric J. Gomez,[†] Karl Gerhardt,[†] Justin Judd,[†] Jeffrey J. Tabor,^{†,‡,§} and Junghae Suh^{*,†,‡}

[†]Department of Bioengineering, [‡]Systems, Synthetic, and Physical Biology Program, and [§]Department of Biochemistry and Cell Biology, Rice University, Houston, Texas 77005, United States

S Supporting Information

ABSTRACT: Gene delivery vectors that are activated by external stimuli may allow improved control over the location and the degree of gene expression in target populations of cells. Light is an attractive stimulus because it does not cross-react with cellular signaling networks, has negligible toxicity, is noninvasive, and can be applied in space and time with unparalleled precision. We used the previously engineered red (R)/far-red (FR) light-switchable protein phytochrome B (PhyB) and its R light dependent interaction partner phytochrome interacting factor 6 (PIF6) from *Arabidopsis thaliana* to engineer an adeno-associated virus (AAV) platform whose gene delivery efficiency is controlled by light. Upon exposure to R light, AAV engineered to display PIF6 motifs on the capsid bind to PhyB tagged with a nuclear localization sequence (NLS), resulting in significantly increased translocation of viruses into the host cell nucleus and overall gene delivery efficiency. By modulating the ratio of R to FR light, the gene delivery efficiency can be tuned to as little as 35% or over 600% of the unengineered AAV. We also demonstrate spatial control of gene delivery using projected patterns of codelivered R and FR light. Overall, our successful use of light-switchable proteins in virus capsid engineering extends these important optogenetic tools into the adjacent realm of nucleic acid delivery and enables enhanced, tunable, and spatially controllable regulation of viral gene delivery. Our current light-triggered viral gene delivery prototype may be broadly useful for genetic manipulation of cells *ex vivo* or *in vivo* in transgenic model organisms, with the ultimate prospect of achieving dose- and site-specific gene expression profiles for either therapeutic (e.g., regenerative medicine) or fundamental discovery research efforts.

KEYWORDS: optogenetics, phytochrome, light-switchable, light-activatable, stimulus-responsive, viral gene delivery, synthetic biology, synthetic virology



Viruses are genetically encoded nanoparticles with regular geometry, monodispersity, and self-assembly. These properties, coupled with an innate ability to infect and deliver nucleic acid cargo into host cells, have fueled efforts toward developing more potent and controllable viral nanoparticles (VNPs) for precision gene delivery applications ranging from fundamental biological studies to clinical translation.^{1,2} However, controlling the specificity and efficiency of delivery remain as considerable challenges limiting the full potential of virus-enabled approaches.³ Many avenues have been pursued to improve the functionality of viruses, yielding a diverse suite of “bionic” viruses that are part natural and part synthetic,⁴ yet more advances are required to transform

naturally occurring viruses into well-controlled and predictable nanodevices.

A promising approach for engineering programmable nanodevices is to encode stimulus-responsive properties. A number of synthetic nanoparticles have been designed such that detection of a particular stimulus leads to a physiochemical change in the nanoparticle, resulting in cargo delivery. For example, chemical ligands,^{5,6} pH,^{7,8} enzymatic reactions,⁹ redox reactions,¹⁰ temperature,^{11,12} and magnetic fields¹³ have served

Received: June 24, 2015

Accepted: November 18, 2015

Published: November 30, 2015

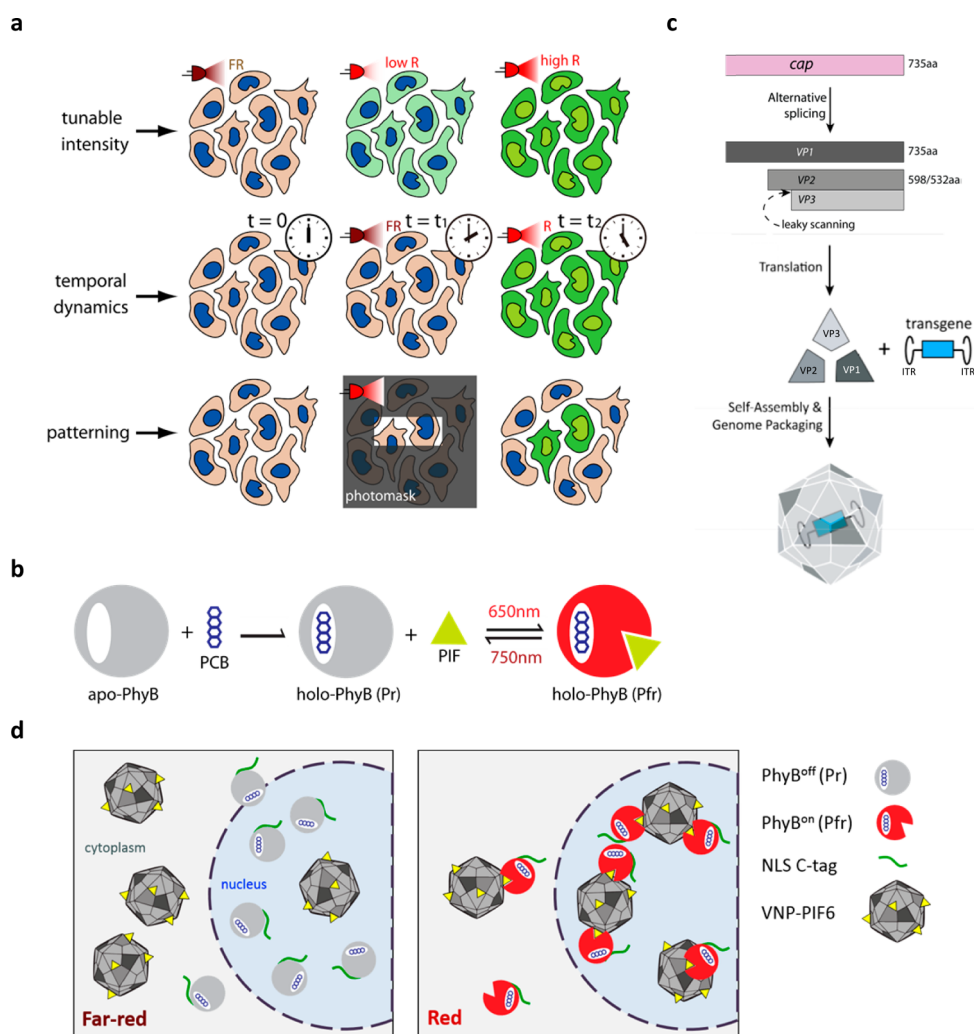


Figure 1. Light-activated viral gene delivery by combining adeno-associated virus (AAV) with the red/far-red (R/FR) light-switchable PhyB/PIF6 system. (a) Light-activated gene delivery would enable refined control of delivery properties. Analog level of expression can be changed by using either activating or deactivating wavelength and modulating intensity (top row), delivery can be delayed or enhanced with time (middle row), and spatial patterning is possible by limiting light exposure using a photomask (bottom row). (b) Phy/PIF are light-switchable binding partners. Apo-PhyB can bind covalently to phycocyanobilin (PCB) to form the photosensitive holoprotein. Holo-PhyB cycles between PIF association and dissociation *via* R (650 nm) and FR (750 nm) light, respectively. (c) The virus capsid proteins VP1–VP3, are encoded in the same ORF of the viral *cap* gene and are differentially transcribed and translated through alternative splicing and leaky scanning. VP1–VP3 self-assemble into a complete 60-mer capsid at a 1:1:10 ratio and will encapsidate genes flanked by inverted terminal repeat sequences (ITRs) up to approximately 4.7 kb in length. (d) Left: VNP-PIF6, an AAV/PIF hybrid, should demonstrate a basal level of nuclear localization in the presence of inactivated PhyB-NLS under FR light or ambient light. Right: Under activating red light, PhyB-NLS should facilitate VNP-PIF6 nuclear internalization and lead to enhanced gene delivery.

as input stimuli for various nonviral nanocarriers. Despite these promising advances, nonviral delivery systems still display lower delivery efficiencies compared to viral vectors. For this reason, we and others have pioneered stimulus-responsive virus-based platforms that respond to pH,¹⁴ chemicals,¹⁵ and extracellular proteases.^{16–18}

Although the use of tissue-specific stimuli may be beneficial for some applications, externally applied stimuli could render the delivery process more quantitatively controllable both in space and time. In particular, light is an attractive stimulus over chemical or biological stimuli because its intensity, duration, spatial pattern, and wavelength can all be precisely modulated in real time with the proper equipment and light configuration.¹⁹ In *in vitro* tissue models, light has been used with resolution on the scale of micrometers to pattern proteins that direct cell processes such as migration and differentiation.^{20,21}

Placing gene delivery under the control of light could enable the same level of spatial resolution with the added benefits of tunable gene product levels and controllable onset of gene expression (Figure 1a).

Light-mediated viral gene delivery has been explored previously using nonengineered viruses or viruses conjugated to photocleavable moieties.^{22,23} Interestingly, simply exposing cells infected by adeno-associated virus (AAV) to UV light increases delivery efficiency, likely by inducing second-strand synthesis of the virus' single-stranded DNA (ssDNA) genome by host cell polymerases.²³ Adenoviral vectors surface-modified with neutralizing moieties that can be removed *via* UV light-activation of photocleavable chemical bonds have enabled site-specific gene expression.²² Although encouraging, UV rays pose health risks (by damaging chromosomal DNA) and fall well outside the red wavelengths wherein light can effectively

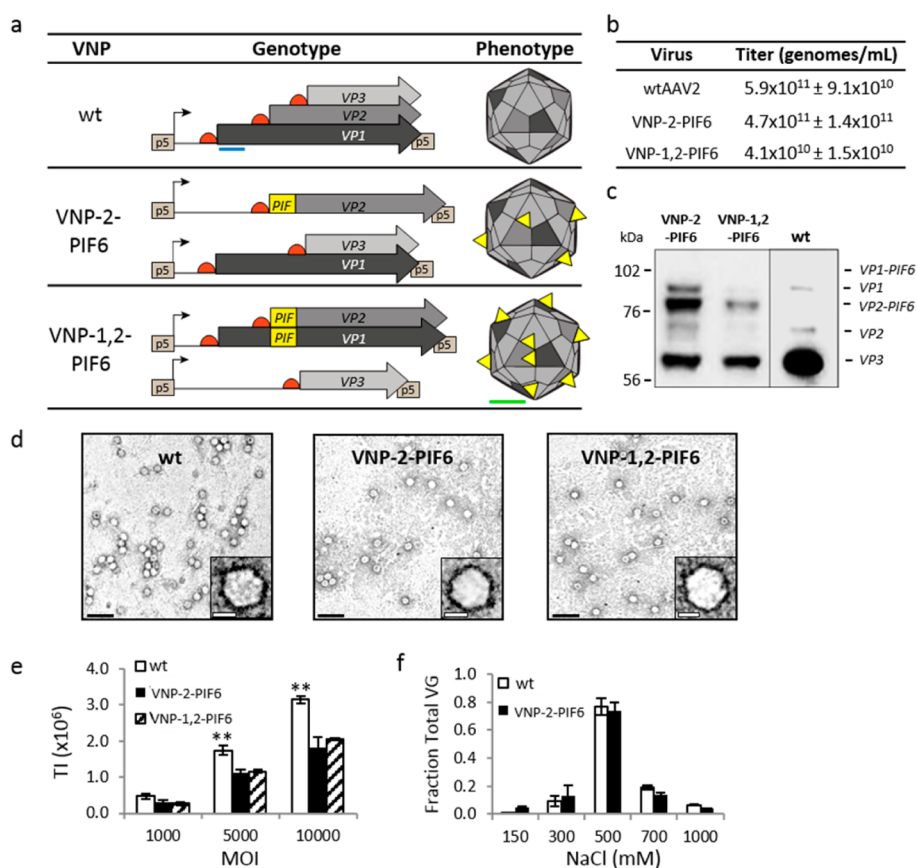


Figure 2. AAV2 tolerates PIF6 insertion in VP2 with native receptor binding affinity but with reduced infectivity. (a) Genetic makeup and resulting capsid structure for wt AAV, VNP-2-PIF6, and VNP-1,2-PIF6. Orange semicircles indicate ribosome binding sites. VP1–VP3 assemble in a 1:1:10 ratio (color-coded). PIF6 is indicated in yellow. All constructs are flanked by p5 promoter/enhancer elements. Blue scale bar = 300 base pairs; green scale bar = 10 nm. (PIF6 not drawn to scale.) (b) Viral titers for wt, VNP-2-PIF6 and VNP-1,2-PIF6. VNP-1,2-PIF6 exhibits a one-log-fold reduction in genome-containing capsids. Average titers from three independent virus batches with corresponding SEM. (c) Western blot with B1 antibody indicates presence of VP2-PIF6 capsid subunit in both VNP-2-PIF6 and VNP-1,2-PIF6 viruses. VP1-PIF6 capsid subunit is not detected in the VNP-1,2-PIF6 virus. (d) Electron micrographs of wt and VNP-PIF6 viruses. VNPs show no distinct morphological differences. Black scale bar = 100 nm, white scale bar = 15 nm. (e) HEK293T cells transduced (multiplicity of infection (MOI): 1000, 5000, or 10 000) with wt, VNP-2-PIF6, and VNP-1,2-PIF6. wt exhibits significantly higher transduction compared to virions harboring PIF6 insertions. Asterisks indicate P value < 0.05 by unpaired Student's t test. Transduction index (TI) is plotted on the y axis and is the product of the percent GFP-positive cells and the geometric mean fluorescence intensity. Error bars are SEM from two independent experiments conducted in triplicate for wt and VNP-2-PIF6, and two independent experiments conducted in duplicate for VNP-1,2-PIF6. (f) Heparin affinity assay shows a statistically similar heparin-binding profiles between wt and VNP-2-PIF6 as determined by two-way ANOVA with Sidak's multiple comparisons test ($n = 2/\text{data point}$, P value = 0.996), indicating no change in native receptor binding due to PIF6 insertion. VNP-1,2-PIF6 was excluded because of a low viral titer. Fraction of total viral genomes quantified by qPCR is plotted on the y axis. Error bars are SEM from two independent experiments conducted in duplicate.

permeate tissue for *in vivo* applications.²⁴ Additionally, chemical conjugation approaches, compared to genetic engineering approaches, can lead to less control of the placement and uniformity of modifications on the viral capsid.

Optogenetics offers a molecular toolbox of light-switchable proteins that remains largely untapped for the development of nanotherapeutics.²⁵ Among the photoswitchable proteins, phytochrome-family proteins are powerful because they can be activated by one wavelength and deactivated by a second wavelength, allowing control over the degree of activation in live cells in space^{26,27} and time.²⁸ For example, phytochrome B (PhyB) has been used for light-switchable transcription,^{29–31} signal-cascade activation,³² actin nucleation,³³ autocatalytic protein splicing,³⁴ pseudopodia elongation,³⁵ and reversible nuclear localization of small proteins in human cells and zebrafish.³⁶ The apo form of PhyB from *Arabidopsis thaliana* covalently binds to the tetrapyrrole chromophore phycocyan-

bilin (PCB) to form the holoprotein, after which PhyB rapidly associates with and dissociates from phytochrome interacting factor 6 (PIF6) upon absorption of red (R, $\lambda_{\text{max}} = 650$ nm) or far-red (FR, $\lambda_{\text{max}} = 750$ nm) photons, respectively (Figure 1b).³⁷ The PhyB/PIF6 system dimerizes in seconds, is amenable to fusion proteins, and is nontoxic to mammalian cells. Thus, we decided to evaluate the usefulness of this heterodimerizing protein pair for rendering the viral gene delivery process responsive to light.

We combined PhyB/PIF6 with one of the most promising gene delivery vectors: AAV, a virus that can deliver genes, short-hairpin RNA, genome-editing zinc-finger endonucleases,³⁸ transcription-activator-like effector nucleases,³⁹ and Cas9 with guide RNAs.^{40–42} AAV consists of a ssDNA genome encapsidated by 60 capsid subunits comprising three different viral proteins (VP1–VP3). The VPs are encoded within the same ORF of the *cap* gene with alternative downstream

initiation sites (Figure 1c). VP1 translates into a 735 amino acid (aa) protein, and VP2/VP3 are truncated alternative splice variants of VP1 missing the N-terminal 137 or 203 aa, respectively. Once translated, VP1–VP3 self-assemble in a 1:1:10 ratio to form the complete 60-mer capsid. AAV naturally infects human cells with relatively high efficiency, and the absence of pathological effects associated with infection has led to its widespread testing for gene therapy applications.⁴³

Even though AAV is considered an efficient gene delivery vector, most virions added to host cells appear to remain outside the nucleus.⁴⁴ In fact, nuclear translocation of delivery vectors is widely recognized as a rate-limiting step and major determinant of effective gene delivery.^{45,46} We hypothesized that we can increase the gene delivery efficiency of AAV by increasing nuclear translocation of the virus. Furthermore, by using light to modulate this key rate-limiting step, the magnitude and spatial distribution of gene delivery may be controllable by an externally applied stimulus. To this end, we developed an optogenetic approach where AAV displays PIF6 on its capsid and PhyB is tagged with a nuclear localization sequence (NLS) such that upon activation with light the PIF6 moieties on the virus bind to PhyB-NLS resulting in tunable nuclear uptake and gene delivery (Figure 1d).

RESULTS AND DISCUSSION

Design Strategy. Although the AAV capsid is amenable to the insertion of proteins and peptides, limitations in insert size and location of insertion have been reported.^{47,48} Levskaia *et al.* constructed a truncated PIF6 conserving the activated phytochrome binding domain (APB) that is only 100 aa and photoreversibly interacts with PhyB in mammalian cells.³⁵ Thus, we first aimed to insert PIF6-APB genetically into the AAV capsid. We generated two different designs, each with PIF6 inserted in a location likely to be displayed on the capsid surface. For wild-type (wt) AAV, the capsid subunits (VP1–VP3) are produced from the same *cap* ORF by alternate mRNA splicing and alternative translation start codon usage (Figure 2a, top row).⁴⁹ Warrington *et al.* created a trans-complementing AAV capsid production scheme where the VP subunits can be expressed individually (or in combination) from separate plasmids.⁴⁸ With this approach, proteins can be inserted in just a subset of the capsid subunits. This trans-complementing approach allows us to separately modify VP1 and VP2 without affecting VP3 because VP3 comprises the majority of the capsid structure and generally does not tolerate protein insertions without compromising virus assembly and function.⁴⁸ Thus, we generated one mutant, VNP-2-PIF6, with PIF6 displayed only on the VP2 capsid subunits, and another mutant, VNP-1,2-PIF6, with PIF6 on VP1 and VP2 capsid subunits (Figure 2a).

To create the VNP-2-PIF6 mutant virus, PIF6 was genetically fused to the N-terminus of VP2 only after methionine residue 138 in *cap*, a location that has been shown previously to tolerate insertion of exogenous proteins and display the insertion on the capsid exterior (Figure 2a, middle row).^{48,50} This site also does not disrupt AAV's binding ability to its cellular receptor, which is heparan sulfate proteoglycan (HSPG) for AAV serotype 2 (AAV2).⁵¹ The VP2 start codon was also mutated from a weak start (ACG) to a strong start (ATG) in order to enhance expression of VP2 and improve the incorporation of the mutant VP2-PIF6 subunit into the assembled capsid.⁴⁸ Analogously, the VNP-1,2-PIF6 mutant virus was generated by first separating the expression of VP1 and VP2 from that of VP3. PIF6 was again inserted after

residue 138, which would result in the fusion of PIF6 to the N-terminus of VP2 as before, but in this case, the VP1 subunit would also harbor the PIF6 insertion 138 residues downstream of its N terminus (Figure 2a, bottom row). The VP2 start codon was mutated to a strong start as in VNP-2-PIF6. Finally, the VP-PIF6 to wt VP plasmid ratio was optimized to produce virus with the highest incorporation of PIF6 and genomic titer. Thus, the two virus designs are engineered forms of the AAV capsid that present surface-exposed PIF6 in either only VP2 or in both VP1 and VP2.

Characterization of VNP-PIF6 Assembly, DNA Packaging, and Transduction. Protein insertions into VNPs can compromise capsid assembly, genome packaging, and transduction (*i.e.*, gene delivery). Even small modifications to the capsid can yield particles with unpredictable and defective phenotypes.⁵² To determine if the AAV capsid tolerates insertion of PIF6 at the above-described locations, the VNP-1,2-PIF6 and VNP-2-PIF6 mutants were evaluated for capsid assembly, genome packaging, and cellular transduction abilities.

To check the production efficiency of the VNP-PIF6 mutants, we transfected HEK 293T cells with the viral production plasmids, harvested the cells, separated the generated viruses from cell debris using density gradient ultracentrifugation, and performed quantitative PCR (qPCR) to measure the genomic titers of viruses produced.⁵³ We observed that VNP-2-PIF6 forms capsids and packages genomes at levels comparable to those of wt, whereas VNP-1,2-PIF6 packages 10-fold less efficiently (Figure 2b). VNP-1,2-PIF6 may exhibit defective production because of protein misfolding or steric difficulties incorporating the unusually large VP1-PIF6 protein into the assembled virus capsid.^{48,54} Western blot analysis using antibodies against the AAV2 capsid subunits suggests successful incorporation of VP2-PIF6 subunits in the assembled VNP-2-PIF6 and VNP-1,2-PIF6 capsids but no detectable incorporation of VP1-PIF6 subunits in the assembled VNP-1,2-PIF6 capsids (Figure 2c), which is likely due to the 1-log-lower viral titer of this mutant. Western blot densitometry analysis on the VNP-2-PIF6 virus indicates a VP stoichiometry of approximately 1:7:22 for VP1/VP2/VP3, suggesting that there are around 14 copies VP2-PIF6 subunits per virus capsid. This shift toward a higher ratio of VP2-PIF6 subunits per capsid is likely due to mutagenizing the VP2 start codon from a weak to a strong start. Transmission electron microscopy (TEM) studies confirmed that both mutants maintain capsid morphologies comparable to wt (Figure 2d).

Next, the transduction efficiencies of the mutants were quantified by applying viruses packaging a GFP transgene to HEK293T cells at multiplicities of infection (MOIs, the virus to cell ratio) of 1000, 5000, and 10 000. After 48 h, the percent GFP-positive and mean fluorescence intensities (MFI) measured by flow cytometry for cells infected by VNP-2-PIF6 and VNP-1,2-PIF6 are consistently lower compared to those of wt (Supporting Information Figure 1). Viruses with PIF6 yield a significantly lower transduction index (the product of the percent GFP-positive cells and geometric MFI)¹⁸ at MOIs greater than 1000 (approximately twofold decrease from wt for both PIF6 viruses at MOI = 10 000, Figure 2e). Prior work by others has also shown decreases in transduction efficiency for mutant AAV vectors with insertions after M138.^{48,50} The defective transduction efficiency of the PIF viruses, however, may be beneficial overall because it may allow for the achievement of a greater dynamic range of transduction (*i.e.*, greatest difference in values comparing transduction before and

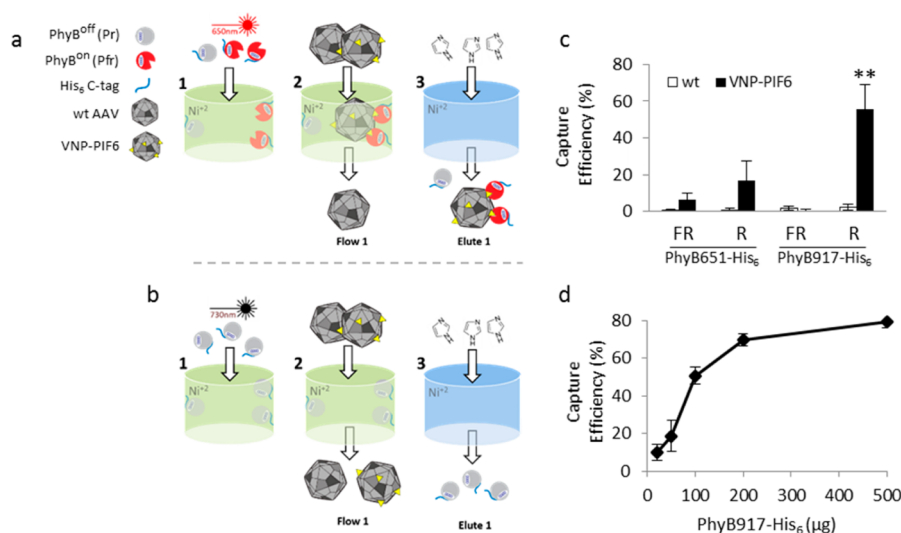


Figure 3. VNP-PIF6 is able to bind activated PhyB *in vitro*. Step 1: PhyB was (a) activated or (b) deactivated and bound to Ni²⁺ via a C-terminal His₆ tag. Step 2: Virus was added to the column under (a) red (R) or (b) far-red (FR) light. Step 3: After several washes, PhyB was eluted out of the column with high imidazole buffer. Column elution fractions from steps 2 and 3 and from wash steps were quantified by real-time PCR. (c) PhyB651 and PhyB917 in the activated (R light) conformation show higher binding to VNP-PIF6 than inactivated PhyB651 and PhyB917 (FR light). Capture efficiency is plotted on the y axis and is the percentage of viral genomes quantified in the elute fractions divided by the total amount of viral genomes added to the column. Error bars are SEM from three independent experiments conducted in duplicate. Asterisks indicate a *P* value < 0.01 by unpaired Student's *t* test. (d) Quantity of column-bound VNP-PIF6 is dependent on amount of PhyB added, and Ni²⁺ columns begin to exhibit saturation after loads of 200 μg of PhyB sample. Error bars are SEM from two independent experiments conducted in duplicate.

after light activation). Although VNP-1,2-PIF6 appears to be as infectious as VNP-2-PIF6, we dropped it from further analysis because of its one-log-lower viral titer and the absence of detectable PIF6 in the VP1 subunit. Thus, only VNP-2-PIF6 was carried forward and is henceforth referred to as VNP-PIF6.

Our design improves virus nuclear localization, which is contingent upon virus entry into the cell, so it is important that PIF6 does not interfere with the virus' ability to bind to its cellular receptor. To assess the receptor binding ability of VNP-PIF6, a heparin-affinity assay was performed. qPCR analysis on heparin-bead elution fractions indicates that PIF6 insertion does not block heparin binding of VNP-PIF6, which exhibits a wt elution profile (Figure 2f). In summary, PIF6 was successfully incorporated into VP2 of assembled viruses with standard production titers and native receptor binding but with attenuated transduction efficiency.

Binding between VNP-PIF6 and PhyB *in Vitro*. To determine if VNP-PIF6 is capable of binding to the activated form of PhyB, we conducted a series of *in vitro* binding assays. Two forms of PhyB, PhyB917-His₆ and PhyB651-His₆, were generated by *Dictyostelium discoideum* or *Escherichia coli* expression, respectively, and purified *via* Ni²⁺ chromatography. Purity of PhyB solutions was checked with Western blot and Coomassie assays (Supporting Information Figure 2). We posited that the smaller size of PhyB651 could be advantageous in the context of binding to PIF6 on the VNP surface because capsid topography could sterically occlude the larger PhyB917 from binding effectively. Conversely, the truncated PhyB651 lacks part of the PHY domain, a motif conserved in all phytochromes that plays a role in the spectroscopic and photochemical properties of the protein.^{32,35,55} PhyB917 retains the entire PHY domain, which is implicated in stabilizing the light-activated form of PhyB.⁵⁶

PhyB651-His₆ or PhyB917-His₆ were first directly exposed to R or FR light for 30 min before being immobilized on a Ni²⁺

column and were left under R or FR for the remainder of the experiment (Figure 3a,b). AAV2 (wt or VNP-PIF6) was then passed through the column (flow fraction), and after two column washes, any Ni²⁺-bound protein was eluted by imidazole competition (elute fraction). qPCR analysis was performed on each fraction to detect the genomic titers of viruses and determine the capture efficiency of PhyB, which is defined as VNP titer in the eluted fractions divided by the total amount of VNPs added to the column. Under deactivating FR light, neither wt nor VNP-PIF6 AAV2 binds to PhyB917 or PhyB651 in an appreciable amounts (Figure 3c). Under activating R light, however, VNP-PIF6 binds PhyB917 24-fold better than does wt AAV2. VNP-PIF6 is also able to bind activated PhyB651 at a 17-fold higher level compared to wt virus. Between the two PhyB variants, PhyB917 possesses a greater dynamic range, capturing 3-fold more VNP-PIF6 than does PhyB651 under activating R light and almost 10-fold less VNP-PIF6 under deactivating FR. Altering the amount of PhyB added to the column changes the amount of VNP-PIF6 captured, indicating that the virus elution profiles are primarily affected by the presence of PhyB and not by nonspecific binding to the column (Figure 3d). Overall, we are able to achieve 80% capture efficiency (about 4 × 10⁹ genome-packaging viruses captured out of 5 × 10⁹) after immobilizing 500 μg of activated PhyB917.

The VNP-PIF6 interaction with PhyB917, once activated with R light, should be reversible by deactivation with FR light. This light-induced dissociation was indeed confirmed with the *in vitro* binding assay (Supporting Information Figure 3a,b). Lastly, the photoswitchable interaction was validated by comparing the binding of VNP-PIF6 to PhyB917 versus a constitutively active PhyB mutant (Supporting Information Figure 3c).⁵⁷ Overall, these results indicate that the light-inducible PhyB-PIF6 interaction is preserved between soluble PhyB and the PIF6 genetically inserted on the virus capsid.

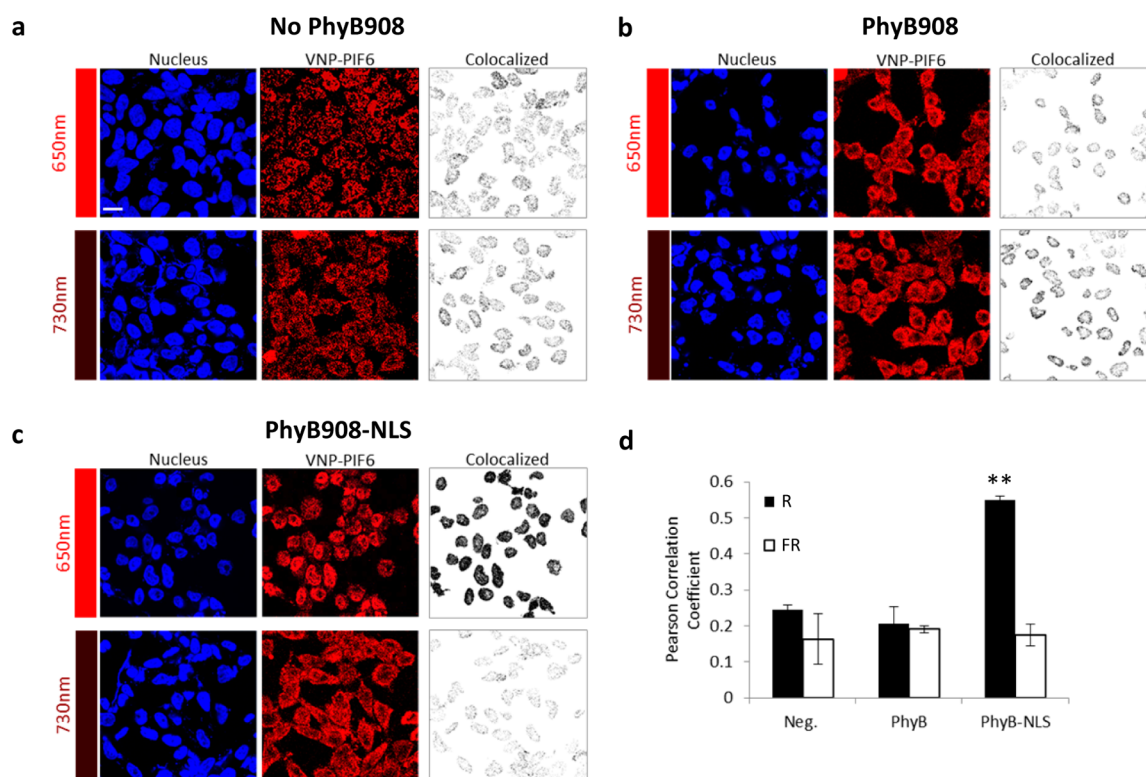


Figure 4. VNP-PIF6 exhibits increased nuclear localization under red (R) light but not under far-red (FR) light in the presence of PhyB-NLS. HeLa cells were transfected with PhyB908 or PhyB908-NLS, and 24 h later, PCB and VNP-PIF6 (MOI: 5000) were added to cells. After 4 h exposure to R or FR light, cells were fixed and stained for immunofluorescence. (a–c) VNP-PIF6 exhibits markedly higher nuclear localization in HeLa cells expressing PhyB-NLS and exposed to R light, compared to cells expressing no PhyB or untagged PhyB or under FR light. Left panel: Hoechst nucleus. Middle panel: A20 anti-AAV2 antibody. Right panel: object-based colocalized pixels. Object-based colocalization was used to segment nuclei and qualitatively determine overlap with A20 signal. Scale bar = 20 μm (d) Pearson correlation coefficient for Hoechst and A20 channels indicates significantly higher correlation between channels only in cells expressing PhyB-NLS under R light. Error bars are SEM from two independent experiments with average cell count of 40 per experiment. Asterisks indicate a P value < 0.001 by unpaired Student's t test.

Light-Induced Nuclear Localization of VNP-PIF6 in Cells Expressing PhyB908-NLS. In gene delivery, the nuclear entry step is recognized as a critical bottleneck to efficient delivery.^{58–60} Although three putative nuclear localization sequences have been identified in the AAV2 capsid,^{59,60} viruses still translocate into the nucleus inefficiently.⁴⁴ We sought not only to overcome the nuclear entry barrier experienced by AAV but also to render this key step in the transduction process light-controllable.

HeLa cells were made to express PhyB908 or PhyB650 (variants analogous to PhyB917 and PhyB651) with or without C-terminal NLS tags. At 24 h later, PCB was added to cell media, followed by addition of VNP-PIF6 or wt AAV2 1 h later. Because previous studies indicate that AAV intracellular trafficking events mostly occur within several hours,⁶¹ cells were exposed to either R or FR light for 4 h before fixation and staining for immunofluorescence studies (Figure 4). Exposing PhyB908-NLS-expressing cells to R light dramatically increases the nuclear accumulation of VNP-PIF6 (Figure 4c, top row). In contrast, in control cells expressing no PhyB, untagged PhyB, or those exposed to FR light, the viruses are mostly in the cytoplasm or aggregated in the perinuclear space (Figure 4a–c).

The colocalization of the VNP signal and the nucleus signal was quantified through image analysis. In particular, the Pearson correlation coefficients and the thresholded Mander's coefficients reveal statistically significant higher colocalization

between VNP-PIF6 and the nucleus only in cells expressing PhyB908-NLS and exposed to activating R light (Figure 4d and Table 1). The truncated PhyB650-NLS (a variant of PhyB651 with an NLS tag) does not affect the intracellular distribution of VNP-PIF6 (Supporting Information Figure 4), possibly reflecting the lower *in vitro* binding observed in Figure 3. The weaker interaction between VNP-PIF6 and PhyB650 may be due to the partial ablation of the PhyB PAS domain, a deletion that was previously shown to result in weaker or complete lack of PhyB binding to PIF6.^{31,35} It is also possible that structural differences at the C-terminal end of the truncated PhyB variant obstruct recognition of the NLS tag by cellular importins.

To confirm that the nuclear localization of VNP-PIF6 is not an artifact of 2D visualization, 3D Z-stacks were obtained with confocal microscopy. Visualizing cell nuclei sliced through the x , y , and z axes (Figure 5a) and closer inspection of y axis individual channel slices (Figure 5b) confirmed higher VNP signal inside the nucleus. 3D reconstructed movies were generated to further visualize the difference in VNP distribution in PhyB908-NLS expressing cells exposed to FR or R light (Supporting Information Movies 1 and 2). These data suggest that VNP-PIF6 selectively binds to activated PhyB908-NLS under physiological conditions, leading to more effective nuclear translocation of VNPs.

Lastly, we evaluated the cell-line-dependent functionality of VNP-PIF6/PhyB908-NLS in different cell types, including

Table 1. Virus–Nucleus Colocalization Statistics

PhyB type	virus	light	tM(nuc) ^a	tM(virus) ^a
none	wt		0.13	0.52
none	VNP-2-PIF6	FR	0.08	0.45
none	VNP-2-PIF6	R	0.07	0.39
PhyB650-NLS	VNP-2-PIF6	FR	0.12	0.47
PhyB650-NLS	VNP-2-PIF6	R	0.10	0.25
PhyB908	VNP-2-PIF6	FR	0.13	0.41
PhyB908	VNP-2-PIF6	R	0.08	0.33
PhyB908-NLS	VNP-2-PIF6	FR	0.06	0.40
PhyB908-NLS	VNP-2-PIF6	R	0.45 ^b	0.64 ^b

^aMander's thresholded colocalization coefficients for HeLa cells infected with wtAAV2 or VNP-PIF6 (MOI: 5000). Measurements were determined over two fields of view for each sample, with an average of 40 cells per field of view. Unlike the Pearson correlation coefficient, Mander's thresholded values are based on signal intensity. tM(nuc) is the proportion of all nuclear signal overlapped by virus signal. tM(virus) is the proportion of all virus signal overlapped by nuclear signal. Nuclear and AAV signals were uniformly thresholded using the ImageJ JACoP plugin. ^bDifferences between colocalization of VNP-PIF6 sample with PhyB-NLS and R light, and all other conditions are statistically significant ($p < 0.05$) by unpaired Student's t test.

those of interest in tissue engineering applications such as human mesenchymal stem cells (hMSC), human umbilical vein endothelial cells (HUVEC), and 3T3 fibroblasts. Compared to wt and VNP-PIF6 AAV under FR light, we recorded significantly higher nuclear colocalization levels for VNP-PIF6 under R light for all three cell lines (Supporting Information Table 1).

Stimulus-Responsive Gene Delivery with VNP-PIF6 Using R/FR Light. Having established enhanced nuclear localization of VNP-PIF6 using activating R light, we set out to evaluate whether modulating R/FR ratio can tune the efficiency of gene delivery. HeLa cells were cultured in a 24-well glass-

bottomed tissue culture plate placed on a 3D-printed platform with Arduino-controlled light-emitting diodes (LEDs) directly underneath each well (Figure 6a). Raw Arduino PWM values used for R (630 nm) and FR (735 nm) LEDs were converted to photon flux using a fiber-optic photodetector (Methods). Cells were transfected with PhyB or PhyB-NLS for constitutive expression, supplemented with PCB and then transduced by VNP-PIF6 carrying a GFP transgene at an MOI of 2000. Although Phy/PIF binding occurs on the order of seconds, studies have used longer illumination times to maximize light-induced output.⁶² Therefore, for the entire cell incubation period, individual wells were illuminated with a range of R and FR intensities resulting in multiple R/FR ratios. At 24 or 48 h later, GFP expression for each experimental condition was visualized using fluorescence microscopy and measured using flow cytometry, and results were compiled to establish a dose–response linking R/FR flux to gene delivery efficiency (quantified as the TI). Pilot tests revealed that PhyB without an NLS tag clearly does not affect gene delivery (Supporting Information Figure 5), so it was omitted from further experiments. Additionally, no significant difference in TI was observed after 24 h post-transduction (Supporting Information Figure 5), so this time point was dropped from further testing. An MTT metabolic activity assay indicates moderate cell line-specific toxicity, warranting future optimization studies to minimize cell death (Supporting Information Figures 6 and 7).

In the absence of R light or PCB, VNP-PIF6 delivers GFP poorly (Figure 6b). Additionally, with PCB under dark conditions or with high intensity FR light only, the VNP-PIF6 virus displays significantly lower TI compared to that of wt AAV (Figure 6c). Dose–response curves for several intensities of codelivered FR light followed the same trend: With increasing intensities of R light, gene delivery by VNP-PIF6 significantly increased (Figure 6c). As expected, increasing intensities of codelivered FR light decreases R-light-activated TI, indicating that FR light can be used to reduce system

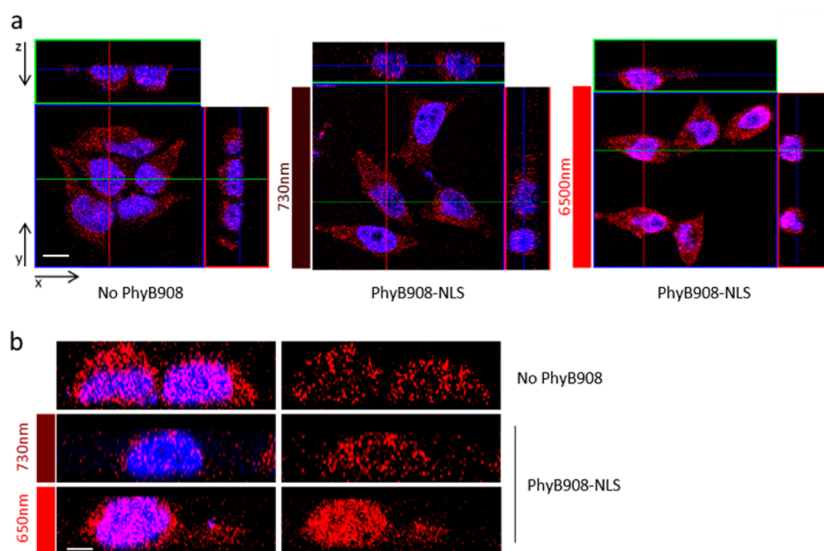


Figure 5. Increased nuclear localization of VNP-PIF6 under red (R) light confirmed *via* confocal 3D imaging. (a) Orthotopic nuclear slice along x , y , and z axes, focused to location indicated by crosshairs, in cells transduced with VNP-PIF6 (MOI: 5000). Left panel: cells without PhyB. Middle panel: cells with PhyB-NLS under far-red light. Right panel: cells with PhyB-NLS under R light. Scale bar = 10 μm . (b) The y axis cross section shows Hoechst and A20 signal (left) or only A20 signal (right) of cells from panel a. A20-only signal is shown for easier visualization of virus intracellular location. Markedly higher virus nuclear localization is evident for PhyB-NLS under R light condition. Scale bar = 4 μm .

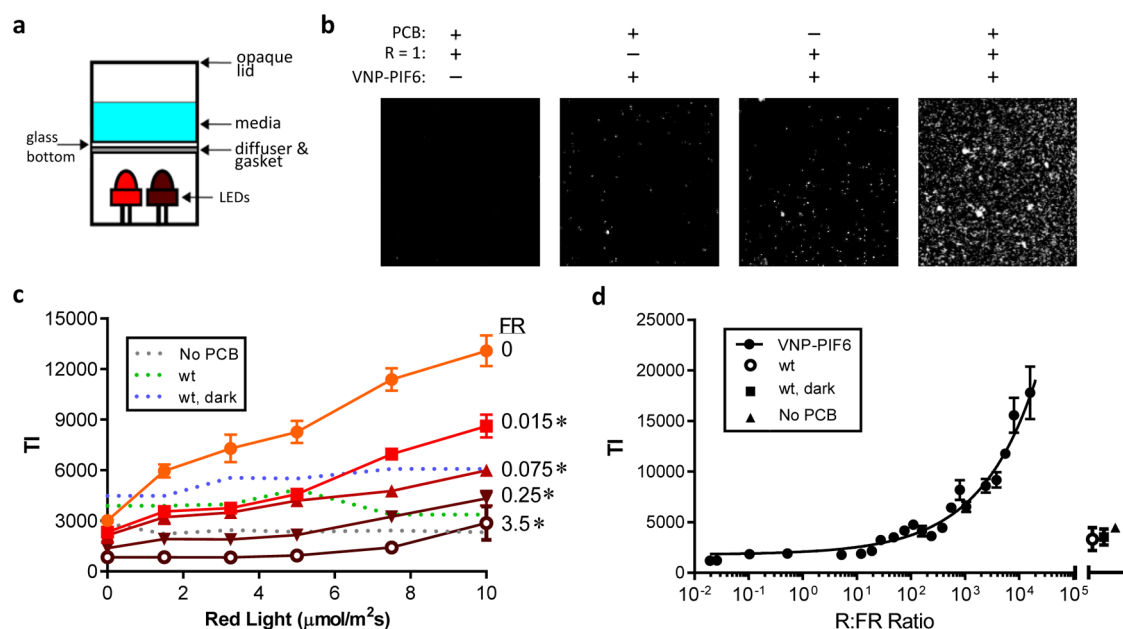


Figure 6. Analog level of gene delivery by VNP-PIF6 can be tuned by codelivered red/far-red (R/FR) light. HeLa cells were seeded into a 24-well plate with opaque walls and lid. Well bottoms are glass and were coated by poly(L-lysine) to facilitate cell adherence before transduction by VNP-PIF6 or wt at an MOI of 2000. LEDs installed directly underneath each well illuminated the cells with R and/or FR light at varying intensities for 48 h before cells were evaluated for GFP fluorescence by fluorescence microscopy or flow cytometry. (a) Schematic of individual well setup in tissue culture plate. (b) Fluorescent micrographs of GFP expression in HeLa cells constitutively expressing PhyB-NLS and treated with or without VNP-PIF6, PCB, and R light. (c) Dose-response curves for transduction by VNP-PIF6 in HeLa cells under increasing R light flux between 0 and 10 $\mu\text{mol}/(\text{m}^2 \text{ s})$, highlighting the effect of increasing codelivered FR light ($\mu\text{mol}/(\text{m}^2 \text{ s})$). Asterisks indicate statistically significant difference in transduction index (TI) compared to FR = 0 control, determined by two-way ANOVA and Tukey's post hoc test ($n = 4/\text{data point}$, $F = 10.81$, P value < 0.001). (d) Full-range logarithmic dose-response curve of transduction index by VNP-PIF6 facilitated by PhyB-NLS under varying R/FR ratios. For each ratiometric data point, different R or FR intensities were used. Data is fit (black line) to the equation $\text{TI} = Ax^B + C$, where $A = 285$, $B = 0.41$, $C = 1800$, and $r^2 = 0.95$. Controls are depicted off-axis on the same TI scale (wt under R/FR = 1000, wt in dark, and VNP-PIF6 without PCB). Each data point represents the average of $n = 4$ or 5 replicates from $N = 2$ independent experiments. Error bars are SEM.

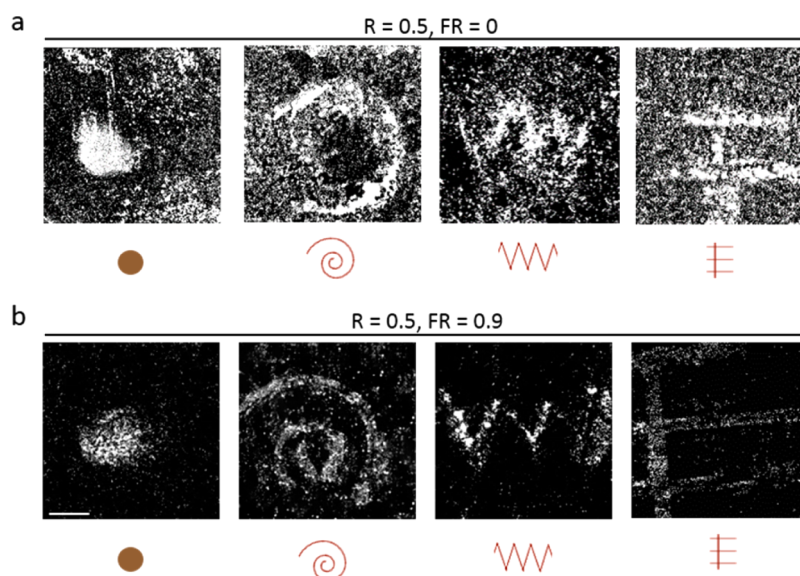


Figure 7. Light-activated spatial patterning of gene expression with VNP-PIF6 using photomasks. HeLa cells expressing PhyB908-NLS were treated with PCB and VNP-PIF6 and exposed to far-red (FR) light for 30 min, followed by exposure to red (R) light only (top row) or R/FR light (bottom row) for 60 min. The numerical values correspond to light flux in units of $\mu\text{mol}/(\text{m}^2 \text{ s})$. Cells were incubated in the dark for the remainder of 48 h. (a) Using R light only leads to a high background in gene expression. Patterns appear incomplete and distorted. (b) Adding FR light lowers the total gene expression but leads to higher signal-to-noise ratio of the desired patterns shown below the micrographs. Photomasks were created in Adobe Illustrator and laser-etched onto black nitrile. Images are 12×12 stitches taken at $20\times$ magnification with an epifluorescence microscope. Scale bar is 2 mm.

sensitivity to activation. At high R/FR ratios, the resulting TI increases with the maximum level of 17 796 achieved at R/FR = 15,950 (Figure 6d). Remarkably, at R/FR ratios greater than ~250, VNP-PIF6 is able to transduce cells more effectively than wt. Therefore, by increasing the number of viruses that translocate into the nucleus, we are able to overcome the almost twofold decrease in transduction efficiency due to PIF6 insertion in the capsid (Figure 2e). Prior work by others has suggested coinfection with adenovirus “helps” AAV transduction by enabling a greater number of AAV particles to enter the nucleus,⁶³ and our findings further support the idea that greater nuclear entry leads to greater transduction efficiency. If the PCB chromophore is not supplied to the cells, then the TI is unaffected by light, further supporting the idea that the observed dose-response curve is mediated by light-responsive PhyB. Our R-light-activatable viral gene delivery platform works in different cell types, including hMSC, HUVEC, and 3T3 fibroblasts (Supporting Information Figure 8).

Interestingly, at R/FR values above 16 000, the TI declines monotonically (Supporting Information Figure 9). Exposing cells to only R light at maximum intensity leads to a relatively low TI that is comparable to background levels achieved with the no PCB controls. Diminishing GFP expression at higher R light intensities could be caused by photolysis of the PCB chromophore.²⁹ Collectively, the results demonstrate our ability to use light as a variable input not only to tune the gene delivery output of AAV but also to achieve dramatically enhanced efficiencies compared to those of wt.

Spatially Controlled Viral Gene Delivery with R/FR Light. For some biomedical applications, spatial control of gene delivery may be an important parameter for achieving the desired therapeutic outcomes. Thus, we next explored the utility of the VNP-PIF/PhyB-NLS system for spatial patterning of gene expression in a population of cells. Photomasks with simple patterns (Figure 7) were laser-etched into black nitrile and secured directly underneath cell culture wells with glass bottoms. Cells expressing PhyB908-NLS were given PCB and VNP-PIF6 (MOI: 1000) and then exposed to FR light for 30 min followed by R light for 1 h,⁶² after which cells remained in the dark for the remainder of 48 h before being fixed for microscopy. Using only R light results in high background noise in gene expression for our system, even for relatively low flux (Figure 7a). However, codelivering FR light results in improved signal-to-noise ratio and better resolved patterns (Figure 7b). These data suggest that optogenetic augmentation of viral vectors can be used to achieve space-resolved gene expression profiles.

CONCLUSIONS

Our optogenetic protein-virus hybrid system addresses the common gene delivery barrier of nuclear entry, but this general approach could in principle be applied to any intracellular trafficking steps. For example, molecular strategies could be developed to control cytoplasmic transport of the viruses with externally applied light. Furthermore, because R and FR light fall within the tissue-penetrating optical window,²⁴ designs such as the one presented in this work could be adapted for *in vivo* applications. Future optimizations to our light-inducible design may improve the functionality of the platform for therapeutic applications. For example, modifications to the prototype vector can be made to improve the overall signal-to-noise by decreasing basal infectivity of virions or allowing presentation of PIF6 in other conformations or locations more amenable to

binding PhyB. Genetic insertion of other recombinant light-sensitive proteins into the virus capsid could enable multi-spectral-responsive gene vectors that are coordinated by several orthogonal light inputs, each controlling a different aspect of virus intracellular trafficking. The need to add or express⁶² the exogenous chromophore PCB and express PhyB-NLS in target tissues renders this strategy premature for clinical gene therapy applications; however, the currently presented platform may be valuable as a tool for gene delivery in *ex vivo* tissue engineering applications, genetic manipulation studies *in vivo* in transgenic model organisms (e.g., transgenic mouse expressing PhyB-NLS), and intracellular virus infection pathway studies *in vitro*. These limitations may be overcome in the future by using other photoresponsive protein modules that use chromophores endogenous to mammalian tissue and promote regulation of virus infectivity without relying on protein dimerization.⁶⁴

In conclusion, by combining light-switchable heterodimerizing proteins from the optogenetics toolbox with AAV, we have created a viral gene delivery platform whose efficiency is controlled by externally applied light. In particular, the system design modulates the nuclear translocation step, a recognized rate-limiting barrier of the delivery process, such that exposure to the activating wavelength of light enables significantly greater numbers of viruses to enter the nucleus. By manipulating the intensities and ratios of activating and deactivating light, we are able to achieve significantly enhanced delivery efficiencies compared to the wt virus. Furthermore, using a simple photomask, we can easily obtain space-resolved gene expression patterns. Our tunable, light-responsive delivery approach may enable fundamental discovery research efforts at a variety of biological length scales, ranging from the study of intracellular viral infection pathways in single cells to the impact of modulating gene expression profiles in live transgenic mouse models. The platform may also be used to control the level and location of transgene expression in a population of cells *ex vivo*, enabling the development of engineered tissue constructs for regenerative medicine applications.

METHODS

Virus Preparation. Recombinant adeno-associated virus serotype 2 (AAV2) was prepared as described previously.⁶⁵ Briefly, using polyethylenimine, HEK293T cells were transfected with pXX2 carrying the AAV2 *rep* and *cap* genes, the adenovirus helper plasmid pXX6-80, and pAV-GFP, encoding green fluorescent protein (GFP) driven by a cytomegalovirus (CMV) promoter. To generate the AAV2 mutant with the 100 aa N terminus of PIF6 fused to the VP2 capsid subunit (VNP-2-PIF6), pXX2 in the transfection mixture was substituted with plasmids pVP2A-PIF6 and pRC_RR_VP1/3¹⁸ in a 4:1 ratio. pVP2A-PIF6, which contains PIF6 inserted at the VP2 N terminus flanked by *Mlu*I and *Eag*I restriction sites, was generated using pVP2A as the starting construct. pVP2A has mutated VP1 and VP3 start codons to prevent their expression, and the weak VP2 start codon (CTG) altered to a strong start (ATG).⁴⁸ For VNP-1,2-PIF6, a similar approach was followed, except that pVP2A was replaced with pVP1,2A to achieve PIF6 fusion to both VP1 and VP2 capsid subunits and pRC_RR_VP1/3 was replaced by pRC_RR_VP3 to supplement wt VP3. HEK293T cells were harvested 48 h after transfection, and virus was separated from cell debris by iodixanol gradient ultracentrifugation. Virus was purified by heparin affinity chromatography with HiTrap Heparin HP columns (GE), and for electron microscopy and cellular studies, virus was then dialyzed into Dulbecco's phosphate-buffered solution (DPBS) with Ca²⁺ and Mg²⁺. Virus titers were measured *via* quantitative polymerase chain reaction (qPCR) with SYBR green (Life Technologies) reporter dye and using primers against the CMV promoter in the GFP transgene cassette: FWD =

TCACGGGGATTCCCAAGTCTC, and REV = AATGGG-CGGGAGTTGTTACGAC.

PhyB Plasmids. For *in vitro* binding studies, PhyB917 from *A. thaliana* was codon-optimized for expression in *Dictyostelium discoideum* (*Dd*). A C-terminal hexahistidine tag was added *via* iterative golden-gate ligation with *Bsa*I sticky ends using the following primers: FW = GCATTAGGTCTCTAATGGTATCTGGTGTGTTG-TGGTTC, REV-1 = ATGATGATGATGATGATGACCA-CCACCCTACTGCAAGAGCTTGTGTAATTCCTGG, and REV-2 = GCTAATGGTCTCTTTTAATGATGATGATGA-TGATGACCACC.

PhyB917-His₆ was cloned by golden-gate ligation into expression vector pDM323 downstream of the constitutive promoter P_{act15}.^{66,67} PhyB917-His₆ was mutated *via* site-directed mutagenesis (Quik-Change, Agilent Genomics) to obtain PhyB917(Y276H)-His₆. PhyB651-His₆ cloned into a pET28a/Tev/His6 vector was obtained from Dr. M. Rosen (UT Southwestern, TX). For studies in cells, pKM216, pKM017, and pKM018 encoding PhyB908, PhyB908-NLS, and PhyB650-NLS, respectively, were obtained from Dr. W. Weber (University of Freiburg, Germany).

In Vitro PhyB Expression and Purification. *Dd* strain AX4 was transformed with plasmids pEG03 and pEG04 encoding PhyB917-His₆ and PhyB917(Y276H)-His₆, respectively, by standard electro- poration protocol.⁶⁸ Single transformants were harvested from *Klebsiella aerogenes*-SM agar plates after 3 days and transferred to liquid HL5 media. Axenic cultures (50 mL, 22 °C, and 180 rpm) were grown to a density of 1 × 10⁷ cells/mL and harvested by centrifugation (500g, 5 min).

PhyB651-His₆ was transformed into *E. coli* strain BL21(DE3) by electroporation and plated onto LB agar containing kanamycin (30 μg/mL) and chloramphenicol (34 μg/mL). Bacteria were then cultured in liquid LB containing kanamycin and chloramphenicol at 18 °C. Cells were induced with 0.5 mM IPTG at OD₆₀₀ = 0.4–0.6 for at least 24 h before being harvested by centrifugation (4000g, 10 min).

Following harvesting by centrifugation, all PhyB variants were separated from cell lysate by repeated freeze/thaw cycles to lyse cells and centrifugation at 3000g for 10 min in the presence of Protease Inhibitor Cocktail (Sigma). Purification from supernatant was performed by nickel-affinity chromatography (His Spintrap, GE Healthcare) according to manufacturer's protocol.

Western Blot of Viruses and PhyB. Viruses and PhyB samples were resolved on 4–12% Bis-TrisNuPAGE gels (Life Technologies) and transferred to nitrocellulose (GE Healthcare) at 40 V for 90 min. Blocking was performed in 5% skim milk in phosphate-buffered saline (PBS) with 0.1% Tween-20 (PBS-T) for 1 h while rocking. Blots were then rinsed three times and rocked for 20 min in PBS-T. Primary antibodies were applied to blots overnight at 4 °C in PBS with 3% BSA (3% BSA-PBS) at the following dilutions: B1 (monoclonal mouse anti-VP1–VP3, three antibodies from American Research Products, diluted 1:50) and anti-His₆ (monoclonal mouse antibody from American Research Products, diluted 1:50). After washing, goat anti-mouse (Jackson ImmunoResearch) peroxidase-conjugated secondary antibody was applied at a 1:2000 dilution in 5% skim milk in PBS-T for 1 h. Blots were then washed three times for 15 min with PBS-T while rocking. Imaging was performed on a Fujifilm LAS 4000 with Lumi-Light Western blotting substrate (Roche).

Electron Microscopy of Virus Capsids. Virus samples purified into DPBS were applied to charged 300-mesh carbon grids (Ted Pella, Redding, CA) for 5 min. Samples were washed and negative-stained with 0.75% uranyl formate to stain viral capsids and imaged on a JEOL 2010 transmission electron microscope operating at 120 kV (JEOL, Tokyo, Japan).

Heparin Binding Assay. Viruses in iodixanol were incubated for 15 min with heparin–agarose beads (Sigma) resuspended in Tris-HCl with 150 mM NaCl. Samples were centrifuged at 6000g for 5 min to pellet beads, and the supernatant was collected. Beads with bound virus were then resuspended sequentially in Tris-HCl containing NaCl at 300, 500, 700, and 1000 mM, with the supernatant collected at each step. Viral genomes collected in each fraction were quantified by qPCR.

Transduction Assay. HEK293T cells were seeded at 1 × 10⁵ cells/well on poly(L-lysine)-coated 48-well plates approximately 30 h before virus was added to cells in serum-free media. Fresh media containing serum was added 4 h post-transduction, and cells were harvested at 48 h for flow cytometry analysis on a BD FACSCanto II. Virus transduction ability was assessed by quantifying the transduction index (TI = % GFP⁺ cells × geometric mean fluorescence intensity), a linear indicator of virus activity.¹⁸

In Vitro Binding Assay. PhyB-His₆ samples were diluted in binding buffer (20 mM NaPO₄, 500 mM NaCl, 20 mM imidazole, pH 7.4) and incubated for 30 min with phycocyanobilin (PCB) at a final concentration of 5 μM under green light (500 nm) to prevent chromophore bleaching and then exposed to either 650 nm (R) or 730 nm (FR) light. PhyB was bound to Ni²⁺ columns (His Spintrap, GE healthcare) *via* centrifugation at 100g for 30 s, and wtAAV2 or VNP-PIF6 diluted in binding buffer was added to the columns in the presence of 650 or 730 nm light. After a 2 min incubation, columns were washed and bound viruses eluted with elution buffer (20 mM NaPO₄, 500 mM NaCl, 500 mM imidazole, pH 7.4) as per the manufacturer's protocol. Viral genomes present in each fraction were quantified by qPCR.

Confocal Microscopy Study. HeLa cells were seeded onto poly(L-lysine)-coated glass coverslips in a 24-well tissue culture plate at a density of 8 × 10⁴ cells per well in Dulbecco's modified Eagle's medium (DMEM) supplemented with 10% fetal bovine serum and 1% penicillin–streptomycin. After 4 h, cells were transfected with polyethylenimine (PEI)-DNA complexes (N/P = 20) encoding PhyB908 with or without a C-terminal NLS fusion. At 24 h later under green light (500 nm), PCB at a final concentration of 15 μM and virus (purified into DPBS with Mg²⁺ and Ca²⁺) at an MOI of 5000 were applied to cells in serum-free media. Cells were then incubated for 4 h at 37 °C, 5% CO₂ under R or FR light.

For immunofluorescence analysis, cells were washed twice with PBS and fixed with 4% paraformaldehyde for 30 min. Next, cells were permeabilized with warm 0.1% Triton for 10 min, washed twice with PBS, and blocked in 3% BSA-PBS for 30 min with rocking. Primary antibody A20 (monoclonal mouse anti-AAV2 intact capsid from American Research Products, diluted 1:125) was added, and cells were incubated overnight at 4 °C with gentle agitation. After washing three times with PBS with 5 min incubations, secondary fluorescent probe goat anti-mouse Alexa Fluor 532 (Thermo Fisher Scientific) was added at 1:250 dilution, and cells were rocked in the dark for 2 h. Cells were washed three times and stained with Hoechst nuclear stain (0.1 μg/mL) for 15 min with rocking in the dark. After washing twice more in PBS, cells were incubated with 4% paraformaldehyde for 15 min and mounted onto glass slides in 3 μL of Fluoromount-G (SouthernBiotech). Samples were imaged on a Zeiss LSM 710 confocal microscope.

Colocalization Analysis. Images were processed using Zen 2010 software (Carl Zeiss MicroImaging) and ImageJ. Colocalization statistics (PCC, tM1, tM2) were computed with the ImageJ JACoP plugin. Qualitative colocalization images were processed using ImageJ.

Light-Emitting Diode Apparatus Experiments. Cellular light experiments were performed with a custom LED–tissue culture plate apparatus that shields each individual well from outside light. An Arduino Uno microcontroller was used to program a 6 × 4 array of optically isolated LEDs (LEDtronics, #L200CWRGB2K-4A-IL; Marubeni: L735-5 AU) that can expose cells to 630 and 735 nm light simultaneously through the bottom of a 24-well, black, glass-bottomed tissue culture plate (Greiner bio-one, #662892). LED intensity was quantified and converted from raw Arduino units by placing a fiber optic photodetector probe (StellarNet Inc., photo-detector #EPP2000 UVN-SR-25 LT-16, probe #F600-UV–vis-SR) directly into tissue culture wells and measuring light flux for a range of intensities of R/FR light. The glass bottom of each well of the tissue culture plate was coated with poly(L-lysine), and HeLa cells were seeded at a density of 1 × 10⁵ cells per well in DMEM supplemented with 10% fetal bovine serum and 1% penicillin–streptomycin. After 24 h, cells were transfected with PEI-DNA (pKM017 and pKM216) complexes encoding PhyB908 with or without a C-terminal NLS

fusion. At 24 h later, under green light, PCB at a final concentration of 15 μM and virus at an MOI of 2000 were applied in DMEM supplemented with 10% serum and incubated at 37 $^{\circ}\text{C}$ and 5% CO_2 . The LEDs were programmed to shine FR light for 5 min before switching to experiment-dependent intensities of R light. Cells were harvested and prepared for flow cytometry on a BD FACSCanto II after 24 or 48 h.

Space-Resolved Gene Expression. Photomask experiments were conducted following a published protocol for space-resolved gene expression.⁶² Briefly, HeLa cells were cultured in a glass-bottomed, poly(L-lysine)-coated 24-well plate (Greiner bio-one, #662892) with opaque walls and ceilings. Photomasks were laser-etched into black nitrile sheets using a Universal X-660 laser cutter platform and placed under wells. The photomask sheet also functioned as a gasket, sealing the 24-well plate directly above R/FR LEDs. HeLa cells were seeded at a density of 1×10^5 cells per well in DMEM supplemented with 10% fetal bovine serum and 1% penicillin–streptomycin. After 24 h, cells were transfected with PEI-DNA (pKM017) complexes encoding PhyB908 with a C-terminal NLS fusion. After 24 h, PCB at a final concentration of 15 μM and virus at an MOI of 1000 were applied under green light in DMEM supplemented with 10% serum and incubated at 37 $^{\circ}\text{C}$ and 5% CO_2 . The LEDs were programmed to shine FR light (2 $\mu\text{mol}/\text{m}^2\text{s}$) for 30 min before switching to experiment-dependent intensities of R or R/FR light for 60 min. Cells remained in the dark for the remainder of 48 h before being fixed with 4% paraformaldehyde in PBS and imaged on a Nikon A1 microscope. Images were taken at 20 \times magnification, and a 12 \times 12 square array of images were stitched together. Image signal and brightness were processed in ImageJ using the Threshold function.

Statistics. All *t* tests were performed in Microsoft Excel. ANOVA analysis was performed in Graphpad Prism software, using two-way ANOVA grouped column function and post hoc testing.

ASSOCIATED CONTENT

Supporting Information

The Supporting Information is available free of charge on the ACS Publications website at DOI: 10.1021/acsnano.5b05558.

Nucleotide sequence for PhyB917-His₆ as well as data showing the following: VNP-PIF6 is defective in transduction; PhyB651 and PhyB917 can be purified *in vitro*; VNP-PIF6 binding to PhyB917 *in vitro* can be reversed with far-red light; wt AAV2 and VNP-PIF6 in the presence of PhyB650-NLS do not exhibit increased nuclear localization; gene expression by VNP-PIF6 is induced by red light in cells expressing PhyB-NLS; cell metabolic activity assay indicates moderate toxicity induced collectively by VNP-PIF6, PhyB, PCB, and light; cell metabolic activity assay for additional cell lines; light-activatable viral gene delivery in three other cell lines; gene delivery by VNP-PIF6 begins to decline at high red light flux; virus-nucleus colocalization statistics for additional cell lines. (PDF)

Intracellular distribution of VNP-PIF6 4 h after transduction in HeLa cells exposed to far-red light. Blue: cell nuclei. Red: VNP-PIF6. (AVI)

Intracellular distribution of VNP-PIF6 4 h after transduction in HeLa cells exposed to red light. Blue: cell nuclei. Red: VNP-PIF6. (AVI)

AUTHOR INFORMATION

Corresponding Author

*E-mail: jsuh@rice.edu.

Present Address

J. J.: Cardiovascular Research Institute, University of California, San Francisco, California 94143, United States.

Author Contributions

E.J.G. helped conceive the project, planned and conducted experiments, and collected and analyzed data. K.G. planned and conducted experiments and analyzed data. J.J. helped conceive the project and helped plan experiments. J.J.T. helped conceive the project and analyzed data. J.S. helped conceive the project, analyzed data, and directed the project.

Notes

The authors declare no competing financial interest.

ACKNOWLEDGMENTS

This material is based upon work supported by a National Academy of Sciences Ford Foundation Fellowship to E.J.G. We acknowledge Dr. Weber of ETH Zurich for donating plasmids encoding PhyB908 and PhyB650 with and without an NLS for mammalian transfection, Dr. Rosen of UT Southwestern for plasmid PhyB651-His₆ for bacterial expression, Dr. Miller and Samantha Paulsen of Rice University for donating hMSC and HUVEC cell lines, and the University of North Carolina at Chapel Hill Gene Therapy Center Vector Core for providing pXX2, pXX6-80, and pAV-GFP.

REFERENCES

- (1) Kotterman, M. A.; Schaffer, D. V. Engineering Adeno-Associated Viruses for Clinical Gene Therapy. *Nat. Rev. Genet.* **2014**, *15*, 445–451.
- (2) Hastie, E.; Samulski, R. J. Adeno-Associated Virus at 50: A Golden Anniversary of Discovery, Research, and Gene Therapy Success—a Personal Perspective. *Hum. Gene Ther.* **2015**, *26*, 257–265.
- (3) Kay, M. A. State-of-the-Art Gene-Based Therapies: The Road Ahead. *Nat. Rev. Genet.* **2011**, *12*, 316–328.
- (4) Guenther, C. M.; Kuypers, B. E.; Lam, M. T.; Robinson, T. M.; Zhao, J.; Suh, J. Synthetic Virology: Engineering Viruses for Gene Delivery. *Wiley Interdiscip. Rev.: Nanomed. Nanobiotechnol.* **2014**, *6*, 548–558.
- (5) Lai, C.-Y.; Trewyn, B. G.; Jeftinija, D. M.; Jeftinija, K.; Xu, S.; Jeftinija, S.; Lin, V. S. Y. A Mesoporous Silica Nanosphere-Based Carrier System with Chemically Removable Cds Nanoparticle Caps for Stimuli-Responsive Controlled Release of Neurotransmitters and Drug Molecules. *J. Am. Chem. Soc.* **2003**, *125*, 4451–4459.
- (6) Cheng, R.; Feng, F.; Meng, F.; Deng, C.; Feijen, J.; Zhong, Z. Glutathione-Responsive Nano-Vehicles as a Promising Platform for Targeted Intracellular Drug and Gene Delivery. *J. Controlled Release* **2011**, *152*, 2–12.
- (7) Zhou, K.; Wang, Y.; Huang, X.; Luby-Phelps, K.; Sumer, B. D.; Gao, J. Tunable, Ultrasensitive Ph-Responsive Nanoparticles Targeting Specific Endocytic Organelles in Living Cells. *Angew. Chem., Int. Ed.* **2011**, *50*, 6109–6114.
- (8) Evans, B. C.; Hocking, K. M.; Kilchrist, K. V.; Wise, E. S.; Brophy, C. M.; Duvall, C. L. An Endosomolytic Nano-Polyplex Platform Technology for Cytosolic Peptide Delivery to Inhibit Pathological Vasoconstriction. *ACS Nano* **2015**, *9*, 5893–5907.
- (9) Patel, K.; Angelos, S.; Dichtel, W. R.; Coskun, A.; Yang, Y.-W.; Zink, J. I.; Stoddart, J. F. Enzyme-Responsive Snap-Top Covered Silica Nanocontainers. *J. Am. Chem. Soc.* **2008**, *130*, 2382–2383.
- (10) Nguyen, T. D.; Liu, Y.; Saha, S.; Leung, K. C.-F.; Stoddart, J. F.; Zink, J. I. Design and Optimization of Molecular Nanovalves Based on Redox-Switchable Bistable Rotaxanes. *J. Am. Chem. Soc.* **2007**, *129*, 626–634.
- (11) Tian, B.; Wang, C.; Zhang, S.; Feng, L.; Liu, Z. Photothermally Enhanced Photodynamic Therapy Delivered by Nano-Graphene Oxide. *ACS Nano* **2011**, *5*, 7000–7009.
- (12) Park, H.; Yang, J.; Lee, J.; Haam, S.; Choi, I.-H.; Yoo, K.-H. Multifunctional Nanoparticles for Combined Doxorubicin and Photothermal Treatments. *ACS Nano* **2009**, *3*, 2919–2926.

- (13) Gao, J.; Zhang, W.; Huang, P.; Zhang, B.; Zhang, X.; Xu, B. Intracellular Spatial Control of Fluorescent Magnetic Nanoparticles. *J. Am. Chem. Soc.* **2008**, *130*, 3710–3711.
- (14) Yang, L.; Bailey, L.; Baltimore, D.; Wang, P. Targeting Lentiviral Vectors to Specific Cell Types *in Vivo*. *Proc. Natl. Acad. Sci. U. S. A.* **2006**, *103*, 11479–11484.
- (15) Hörner, M.; Kaufmann, B.; Cotugno, G.; Wiedtke, E.; Büning, H.; Grimm, D.; Weber, W. A Chemical Switch for Controlling Viral Infectivity. *Chem. Commun.* **2014**, *50*, 10319–10322.
- (16) Schneider, R.; Medvedovska, Y.; Hartl, I.; Voelker, B.; Chadwick, M.; Russell, S.; Cichutek, K.; Buchholz, C. Directed Evolution of Retroviruses Activatable by Tumour-Associated Matrix Metalloproteases. *Gene Ther.* **2003**, *10*, 1370–1380.
- (17) Ho, M. L.; Judd, J.; Kuypers, B. E.; Yamagami, M.; Wong, F. F.; Suh, J. Efficiency of Protease-Activatable Virus Nanonodes Tuned through Incorporation of Wild-Type Capsid Subunits. *Cell. Mol. Bioeng.* **2014**, *7*, 334–343.
- (18) Judd, J.; Ho, M. L.; Tiwari, A.; Gomez, E. J.; Dempsey, C.; Van Vliet, K.; Igoshin, O. A.; Silberg, J. J.; Agbandje-McKenna, M.; Suh, J. Tunable Protease-Activatable Virus Nanonodes. *ACS Nano* **2014**, *8*, 4740–4746.
- (19) Olson, E. J.; Tabor, J. J. Optogenetic Characterization Methods Overcome Key Challenges in Synthetic and Systems Biology. *Nat. Chem. Biol.* **2014**, *10*, 502–511.
- (20) Wylie, R.; Ahsan, S.; Aizawa, Y.; Maxwell, K.; Morshead, C.; Shoichet, M. Spatially-Controlled Simultaneous Patterning of Multiple Growth Factors in Three-Dimensional Hydrogels. *Nat. Mater.* **2011**, *10*, 799–806.
- (21) Mosiewicz, K. A.; Kolb, L.; van der Vlies, A. J.; Martino, M. M.; Lienemann, P. S.; Hubbell, J. A.; Ehrbar, M.; Lutolf, M. P. *In Situ* Cell Manipulation through Enzymatic Hydrogel Photopatterning. *Nat. Mater.* **2013**, *12*, 1072–1078.
- (22) Pandori, M. W.; Hobson, D. A.; Olejnik, J.; Krzymanska-Olejnik, E.; Rothschild, K. J.; Palmer, A. A.; Phillips, T. J.; Sano, T. Photochemical Control of the Infectivity of Adenoviral Vectors Using a Novel Photocleavable Biotinylation Reagent. *Chem. Biol.* **2002**, *9*, 567–573.
- (23) Ulrich-Vinther, M.; Maloney, M. D.; Goater, J. J.; Soballe, K.; Goldring, M. B.; O'Keefe, R. J.; Schwarz, E. M. Light-Activated Gene Transduction Enhances Adeno-Associated Virus Vector-Mediated Gene Expression in Human Articular Chondrocytes. *Arthritis Rheum.* **2002**, *46*, 2095–2104.
- (24) Anderson, R. R.; Parrish, J. A. The Optics of Human Skin. *J. Invest. Dermatol.* **1981**, *77*, 13–19.
- (25) Sample, V.; Mehta, S.; Zhang, J. Genetically Encoded Molecular Probes to Visualize and Perturb Signaling Dynamics in Living Biological Systems. *J. Cell Sci.* **2014**, *127*, 1151–1160.
- (26) Levsikaya, A.; Chevalier, A. A.; Tabor, J. J.; Simpson, Z. B.; Lavery, L. A.; Levy, M.; Davidson, E. A.; Scouras, A.; Ellington, A. D.; Marcotte, E. M.; Voigt, C. A. Synthetic Biology: Engineering *Escherichia Coli* to See Light. *Nature* **2005**, *438*, 441–442.
- (27) Tabor, J. J.; Levsikaya, A.; Voigt, C. A. Multichromatic Control of Gene Expression in *Escherichia Coli*. *J. Mol. Biol.* **2011**, *405*, 315–324.
- (28) Olson, E. J.; Hartsough, L. A.; Landry, B. P.; Shroff, R.; Tabor, J. J. Characterizing Bacterial Gene Circuit Dynamics with Optically Programmed Gene Expression Signals. *Nat. Methods* **2014**, *11*, 449–455.
- (29) Shimizu-Sato, S.; Huq, E.; Tepperman, J. M.; Quail, P. H. A Light-Switchable Gene Promoter System. *Nat. Biotechnol.* **2002**, *20*, 1041–1044.
- (30) Miliias-Argeitis, A.; Summers, S.; Stewart-Ornstein, J.; Zuleta, I.; Pincus, D.; El-Samad, H.; Khammash, M.; Lygeros, J. In Silico Feedback for *in Vivo* Regulation of a Gene Expression Circuit. *Nat. Biotechnol.* **2011**, *29*, 1114–1116.
- (31) Müller, K.; Engesser, R.; Metzger, S.; Schulz, S.; Kämpf, M. M.; Busacker, M.; Steinberg, T.; Tomakidi, P.; Ehrbar, M.; Nagy, F.; et al. A Red/Far-Red Light-Responsive Bi-Stable Toggle Switch to Control Gene Expression in Mammalian Cells. *Nucleic Acids Res.* **2013**, *41*, e77.
- (32) Toettcher, J. E.; Weiner, O. D.; Lim, W. A. Using Optogenetics to Interrogate the Dynamic Control of Signal Transmission by the Ras/Erk Module. *Cell* **2013**, *155*, 1422–1434.
- (33) Toettcher, J. E.; Gong, D.; Lim, W. A.; Weiner, O. D. Light-Based Feedback for Controlling Intracellular Signaling Dynamics. *Nat. Methods* **2011**, *8*, 837–839.
- (34) Tyszkiewicz, A. B.; Muir, T. W. Activation of Protein Splicing with Light in Yeast. *Nat. Methods* **2008**, *5*, 303–305.
- (35) Levsikaya, A.; Weiner, O. D.; Lim, W. A.; Voigt, C. A. Spatiotemporal Control of Cell Signalling Using a Light-Switchable Protein Interaction. *Nature* **2009**, *461*, 997–1001.
- (36) Beyer, H. M.; Juillot, S.; Herbst, K.; Samodelov, S. L.; Müller, K.; Schamel, W. W.; Römer, W.; Schäfer, E.; Nagy, F.; Strähle, U.; et al. Red Light-Regulated Reversible Nuclear Localization of Proteins in Mammalian Cells and Zebrafish. *ACS Synth. Biol.* **2015**, *4*, 951–958.
- (37) Rockwell, N. C.; Su, Y.-S.; Lagarias, J. C. Phytochrome Structure and Signaling Mechanisms. *Annu. Rev. Plant Biol.* **2006**, *57*, 837.
- (38) Ellis, B.; Hirsch, M.; Porter, S.; Samulski, R.; Porteus, M. Zinc-Finger Nuclease-Mediated Gene Correction Using Single Aav Vector Transduction and Enhancement by Food and Drug Administration-Approved Drugs. *Gene Ther.* **2013**, *20*, 35–42.
- (39) Smith, C.; Gore, A.; Yan, W.; Abalde-Atristain, L.; Li, Z.; He, C.; Wang, Y.; Brodsky, R. A.; Zhang, K.; Cheng, L.; Ye, Z. Whole-Genome Sequencing Analysis Reveals High Specificity of Crispr/Cas9 and Talen-Based Genome Editing in Human Ipscs. *Cell Stem Cell* **2014**, *15*, 12–13.
- (40) Alexander, I.; Russell, D. The Potential of Aav-Mediated Gene Targeting for Gene and Cell Therapy Applications. *Current Stem Cell Reports* **2015**, *1*, 16–22.
- (41) Senis, E.; Fatouros, C.; Große, S.; Wiedtke, E.; Niopek, D.; Mueller, A. K.; Börner, K.; Grimm, D. Crispr/Cas9-Mediated Genome Engineering: An Adeno-Associated Viral (Aav) Vector Toolbox. *Biotechnol. J.* **2014**, *9*, 1402–1412.
- (42) Platt, R. J.; Chen, S.; Zhou, Y.; Yim, M. J.; Swiech, L.; Kempton, H. R.; Dahlman, J. E.; Parnas, O.; Eisenhaure, T. M.; Jovanovic, M.; et al. Crispr-Cas9 Knockin Mice for Genome Editing and Cancer Modeling. *Cell* **2014**, *159*, 440–455.
- (43) Mueller, C.; Flotte, T. R. Clinical Gene Therapy Using Recombinant Adeno-Associated Virus Vectors. *Gene Ther.* **2008**, *15*, 858–863.
- (44) Ding, W.; Zhang, L.; Yan, Z.; Engelhardt, J. F. Intracellular Trafficking of Adeno-Associated Viral Vectors. *Gene Ther.* **2005**, *12*, 873–80.
- (45) Petros, R. A.; DeSimone, J. M. Strategies in the Design of Nanoparticles for Therapeutic Applications. *Nat. Rev. Drug Discovery* **2010**, *9*, 615–627.
- (46) Waehler, R.; Russell, S. J.; Curiel, D. T. Engineering Targeted Viral Vectors for Gene Therapy. *Nat. Rev. Genet.* **2007**, *8*, 573–587.
- (47) Muzyczka, N.; Warrington, K. H., Jr Custom Adeno-Associated Virus Capsids: The Next Generation of Recombinant Vectors with Novel Tropism. *Hum. Gene Ther.* **2005**, *16*, 408–416.
- (48) Warrington, K. H.; Gorbatyuk, O. S.; Harrison, J. K.; Opie, S. R.; Zolotukhin, S.; Muzyczka, N. Adeno-Associated Virus Type 2 Vp2 Capsid Protein Is Nonessential and Can Tolerate Large Peptide Insertions at Its N Terminus. *J. Virol.* **2004**, *78*, 6595–6609.
- (49) Becerra, S.; Koczot, F.; Fabisch, P.; Rose, J. A. Synthesis of Adeno-Associated Virus Structural Proteins Requires Both Alternative Mrna Splicing and Alternative Initiations from a Single Transcript. *J. Virol.* **1988**, *62*, 2745–2754.
- (50) Lux, K.; Goerlitz, N.; Schlemminger, S.; Perabo, L.; Goldnau, D.; Endell, J.; Leike, K.; Kofler, D. M.; Finke, S.; Hallek, M.; Büning, H. Green Fluorescent Protein-Tagged Adeno-Associated Virus Particles Allow the Study of Cytosolic and Nuclear Trafficking. *J. Virol.* **2005**, *79*, 11776–11787.
- (51) Summerford, C.; Samulski, R. J. Membrane-Associated Heparan Sulfate Proteoglycan Is a Receptor for Adeno-Associated Virus Type 2 Virions. *J. Virol.* **1998**, *72*, 1438–1445.
- (52) Shi, W.; Arnold, G. S.; Bartlett, J. S. Insertional Mutagenesis of the Adeno-Associated Virus Type 2 (Aav2) Capsid Gene and

Generation of Aav2 Vectors Targeted to Alternative Cell-Surface Receptors. *Hum. Gene Ther.* **2001**, *12*, 1697–1711.

(53) Rohr, U.-P.; Heyd, F.; Neukirchen, J.; Wulf, M.-A.; Queitsch, I.; Kroener-Lux, G.; Steidl, U.; Fenk, R.; Haas, R.; Kronenwett, R. Quantitative Real-Time Pcr for Titration of Infectious Recombinant Aav-2 Particles. *J. Virol. Methods* **2005**, *127*, 40–45.

(54) Yang, Q.; Mamounas, M.; Yu, G.; Kennedy, S.; Leaker, B.; Merson, J.; Wong-Staal, F.; Yu, M.; Barber, J. R. Development of Novel Cell Surface Cd34-Targeted Recombinant Adenoassociated Virus Vectors for Gene Therapy. *Hum. Gene Ther.* **1998**, *9*, 1929–1937.

(55) Leung, D. W.; Otomo, C.; Chory, J.; Rosen, M. K. Genetically Encoded Photoswitching of Actin Assembly through the Cdc42-Wasp-Arp2/3 Complex Pathway. *Proc. Natl. Acad. Sci. U. S. A.* **2008**, *105*, 12797–12802.

(56) Burgie, E. S.; Bussell, A. N.; Walker, J. M.; Dubiel, K.; Vierstra, R. D. Crystal Structure of the Photosensing Module from a Red/Far-Red Light-Absorbing Plant Phytochrome. *Proc. Natl. Acad. Sci. U. S. A.* **2014**, *111*, 10179–10184.

(57) Fischer, A. J.; Rockwell, N. C.; Jang, A. Y.; Ernst, L. A.; Waggoner, A. S.; Duan, Y.; Lei, H.; Lagarias, J. C. Multiple Roles of a Conserved Gaf Domain Tyrosine Residue in Cyanobacterial and Plant Phytochromes. *Biochemistry* **2005**, *44*, 15203–15215.

(58) Mastrobattista, E.; van der Aa, M. A. E. M.; Hennink, W. E.; Crommelin, D. J. A. Artificial Viruses: A Nanotechnological Approach to Gene Delivery. *Nat. Rev. Drug Discovery* **2006**, *5*, 115–121.

(59) Grieger, J. C.; Snowdy, S.; Samulski, R. J. Separate Basic Region Motifs within the Adeno-Associated Virus Capsid Proteins Are Essential for Infectivity and Assembly. *J. Virol* **2006**, *80*, 5199–5210.

(60) Johnson, J. S.; Li, C.; DiPrimio, N.; Weinberg, M. S.; McCown, T. J.; Samulski, R. J. Mutagenesis of Adeno-Associated Virus Type 2 Capsid Protein Vp1 Uncovers New Roles for Basic Amino Acids in Trafficking and Cell-Specific Transduction. *J. Virol* **2010**, *84*, 8888–8902.

(61) Seisenberger, G.; Ried, M. U.; Endress, T.; Buning, H.; Hallek, M.; Brauchle, C. Real-Time Single-Molecule Imaging of the Infection Pathway of an Adeno-Associated Virus. *Science* **2001**, *294*, 1929–1932.

(62) Müller, K.; Zurbriggen, M. D.; Weber, W. Control of Gene Expression Using a Red- and Far-Red Light-Responsive Bi-Stable Toggle Switch. *Nat. Protoc.* **2014**, *9*, 622–632.

(63) Xiao, W.; Warrington, K. H.; Hearing, P.; Hughes, J.; Muzyczka, N. Adenovirus-Facilitated Nuclear Translocation of Adeno-Associated Virus Type 2. *J. Virol* **2002**, *76*, 11505–11517.

(64) Niopek, D.; Benzinger, D.; Roensch, J.; Draebing, T.; Wehler, P.; Eils, R.; Di Ventura, B. Engineering Light-Inducible Nuclear Localization Signals for Precise Spatiotemporal Control of Protein Dynamics in Living Cells. *Nat. Commun.* **2014**, *5*, 4404 DOI: [10.1038/ncomms5404](https://doi.org/10.1038/ncomms5404).

(65) Xiao, X.; Li, J.; Samulski, R. J. Production of High-Titer Recombinant Adeno-Associated Virus Vectors in the Absence of Helper Adenovirus. *J. Virol.* **1998**, *72*, 2224–2232.

(66) Veltman, D. M.; Akar, G.; Bosgraaf, L.; Van Haastert, P. J. A New Set of Small, Extrachromosomal Expression Vectors for Dictyostelium Discoideum. *Plasmid* **2009**, *61*, 110–118.

(67) Engler, C.; Gruetzner, R.; Kandzia, R.; Marillonnet, S. Golden Gate Shuffling: A One-Pot DNA Shuffling Method Based on Type IIs Restriction Enzymes. *PLoS One* **2009**, *4*, e5553.

(68) Gaudet, P.; Pilcher, K. E.; Fey, P.; Chisholm, R. L. Transformation of Dictyostelium Discoideum with Plasmid DNA. *Nat. Protoc.* **2007**, *2*, 1317–1324.

NOTE ADDED AFTER ASAP PUBLICATION

This paper published ASAP on 11/30/15. The Acknowledgment section was modified and the revised version was reposted on 1/26/16.